



This is a repository copy of *3D inkjet printed self-propelled motors for micro-stirring*.

White Rose Research Online URL for this paper:

<https://eprints.whiterose.ac.uk/188851/>

Version: Published Version

---

**Article:**

Kumar, P. [orcid.org/0000-0002-9965-8691](https://orcid.org/0000-0002-9965-8691), Zhang, Y., Ebbens, S.J. [orcid.org/0000-0002-4727-4426](https://orcid.org/0000-0002-4727-4426) et al. (1 more author) (2022) 3D inkjet printed self-propelled motors for micro-stirring. *Journal of Colloid and Interface Science*, 623. pp. 96-108. ISSN 0021-9797

<https://doi.org/10.1016/j.jcis.2022.05.011>

---

**Reuse**

This article is distributed under the terms of the Creative Commons Attribution (CC BY) licence. This licence allows you to distribute, remix, tweak, and build upon the work, even commercially, as long as you credit the authors for the original work. More information and the full terms of the licence here:

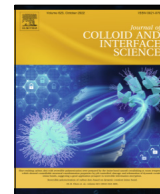
<https://creativecommons.org/licenses/>

**Takedown**

If you consider content in White Rose Research Online to be in breach of UK law, please notify us by emailing [eprints@whiterose.ac.uk](mailto:eprints@whiterose.ac.uk) including the URL of the record and the reason for the withdrawal request.



[eprints@whiterose.ac.uk](mailto:eprints@whiterose.ac.uk)  
<https://eprints.whiterose.ac.uk/>



## 3D inkjet printed self-propelled motors for micro-stirring

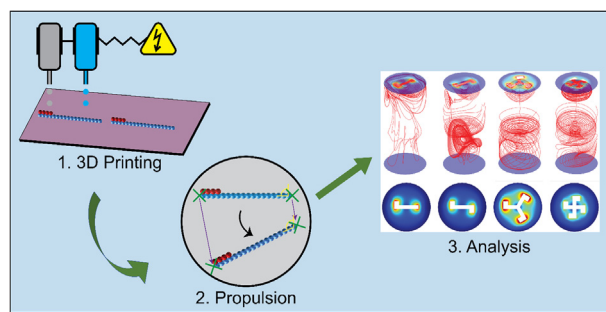
Piyush Kumar<sup>a</sup>, Yi Zhang<sup>a</sup>, Stephen J. Ebbens<sup>a,\*</sup>, Xiubo Zhao<sup>a,b,\*</sup>

<sup>a</sup>Department of Chemical and Biological Engineering, University of Sheffield, Sheffield S1 3JD, UK

<sup>b</sup>School of Pharmacy, Changzhou University, Changzhou 213164, China



### GRAPHICAL ABSTRACT



### ARTICLE INFO

#### Article history:

Received 1 February 2022

Revised 21 February 2022

Accepted 2 May 2022

Available online 5 May 2022

#### Keywords:

Inkjet printing

Bioprinting

Biomaterials

Silk

Biomedical assay

Self-propulsion

### ABSTRACT

**Hypothesis:** Microscopic self-propelled motors (SPMs) are an area of active research, but very little investigation has been conducted on millimetre-scale or macroscopic SPMs and exploring their potential in biomedical research. In this study, we tested if 3D reactive inkjet (RIJ) printing could be used for precise fabrication of millimetre-scale self-propelled motors (SPMs) with well-defined shapes from regenerated silk fibroin (RSF) by converting water soluble RSF (silk I) to insoluble silk fibroin (silk II). Secondly, we compared the different propulsion behaviour of the SPMs to put forward the best geometry and propulsion mechanism for potential applications in enhancing the sensitivity of diffusion-rate limited biomedical assays by inducing fluid flow.

**Experiments:** SPMs with four different geometric shapes and propelled by two different mechanisms (catalysis and surface tension gradient) were fabricated by 3D RIJ printing and compared. For bubble propulsion, the structures were selectively doped in specific regions with the enzyme catalase in order to produce motion via bubble generation and detachment in hydrogen peroxide solutions. For surface tension propulsion, PEG<sub>400</sub>-doped structures were propelled through surface tension gradients caused by leaching of PEG<sub>400</sub> surfactant in deionized water.

**Findings:** The results demonstrated the ability of 3D inkjet printing to fabricate SPMs with desired propulsion mechanism and fine-tune the propulsion by precisely fabricating the different geometric shapes. The resulting 3D structures were capable of generating motion without external actuation, thereby enabling applications in biomedicine such as micro-stirring small fluid volumes to enhance biological assay sensitivity. The surface tension gradient caused by the leaching of surfactant led to faster propulsion velocities with smooth deceleration, whereas, in comparison, catalysis-induced bubble propulsion tended to be jerky and uneven in deceleration, and therefore less suitable for aforementioned

\* Corresponding authors.

E-mail addresses: [s.ebbens@sheffield.ac.uk](mailto:s.ebbens@sheffield.ac.uk) (S.J. Ebbens), [xiubo.zhao@cczu.edu.cn](mailto:xiubo.zhao@cczu.edu.cn) (X. Zhao).

applications. Computational fluid dynamic simulations were used to compare the various experimental SPMs ability to enhance mixing when deployed within 96-well plate microwells, to reveal the effect of both SPM shape and motion character on performance, and show viability for small scale mixing applications.

© 2022 The Authors. Published by Elsevier Inc. This is an open access article under the CC BY license (<http://creativecommons.org/licenses/by/4.0/>).

## 1. Introduction

Self-propulsion is the ability of an object or particle to generate its own movement in a fluid medium by employing a variety of physical and chemical propulsion mechanisms. Learning from the naturally existing self-propelling systems, a wide variety of artificial self-propelled motors (SPMs) have been developed over the past few decades for various applications [1–8]. While many propulsion mechanisms rely on external energy utilised in the form of temperature gradient, light, sound, magnetic and electric fields, the others are instituted by the components contained within the SPMs themselves [9–13].

One old and historically significant example of SPMs are the surface tension driven camphor ‘boats’ [14,15]. First scientifically documented in the 17th century, it took nearly two centuries to fully understand that the phenomenon of self-propulsion of camphor particles on water surface occurs due to the surface tension gradient generated as the camphor dissolves [16]. This phenomenon, called the Marangoni effect, occurs due to the different parts of the fluid surface momentarily having different surface tensions, thus resulting in a gradient in the stress force [17,18]. Within such a gradient, matter on a fluid surface shows the tendency to travel to regions of higher surface tension, causing self-propulsion [18–22].

Chemical reactions with dissolved species at the surface of the object undergoing propulsion provide another approach, that in common with surface tension, doesn’t require derivation of energy from the surroundings [23]. Chemical reactions can lead to a variety of interfacial phenomena that set the particles in motion [24]. Previous studies have investigated many different SPMs utilising enzymes, catalysts, photocatalytic reactions and other non-catalytic chemical reactions which are propelled by the interfacial phenomena of self-diffusiophoresis, and self-electrophoresis [1–4,25,26]. Another possibility for surface catalysis reactions with gaseous products is that motion is generated via bubble production at the surface of the SPM. This requires that the gas bubbles frequently detach or rupture to yield thrust. A common example is catalase induced decomposition of hydrogen peroxide into water and oxygen, which can generate oxygen bubbles once the solution’s local oxygen solubility limit is exceeded, followed by bubble rupture [5,27].

Self-propulsion is an active area of research in order to design and manufacture artificial SPMs with desired characteristics and controllability with their size ranging from a few nanometres to a few centimetres [7,28,29]. Such custom-made SPMs find several applications in biomedical research [30–32], such as diagnoses of medical conditions with lab-on-a-chip devices [33], loading and *in vivo* targeted delivery of therapeutics [34], cancer treatment [35], and catalytic degradation of biologically dangerous chemicals [4]. Observing the propulsion behaviour of SPMs in different fluids can also help in determining unknown parameters, such as, viscosity, surface tension and Marangoni force of a fluid [8,36]. Depending on the application, it is desirable to produce SPMs that undergo specific propulsion behaviour, such as long linear trajectories for payload transport or rotational trajectories for inducing fluid flow in microwells [37,38]. Though prolonged rotational propulsion have been achieved with centimetre-sized self-propelling motors

for different applications, such as generation of electrical energy [39], the millimetre-sized and 3D inkjet-printed self-propelling motors offer a better solution for not only conducting micro-stirring in small well plates, but also achieving geometric complexity and diversity for a better comparison of propulsion efficiency of different motors. The focus in this study is on rotational motion for micro-mixing or stirring of fluids in the microwells used in biomedical assays for the potential enhancement of their sensitivity and finding out how different geometric shapes and propulsion mechanisms alter the motion character and which is the best out of the tested alternatives for use in inducing rapid and consistent fluid flow in microwells.

As the existing SPMs are quite diverse, there is no single established method for their fabrication [28]. However, for biomedical applications, it is essential to use a material which is easily available, inexpensive, biocompatible, biodegradable, and allows easy fabrication of the required SPMs [40]. *Bombyx mori* silk fibroin is one such FDA-approved biomaterial that fulfils all these parameters [41]. In the present study, millimetre-sized SPMs were fabricated from regenerated silk fibroin (RSF) using 3D reactive inkjet bioprinting. This approach made it simple to manufacture SPMs in a variety of shapes and design configurations defined by computer-aided design (CAD), thus allowing easier and more accurate controllability on the desired motion during practical applications [27,42]. The use of inkjet printing for manufacturing micro-stirring motors also opens the door for the highly versatile production of SPMs from such materials as fibroin, which can not otherwise be deposited or fabricated very neatly through other means.

In the present study, two physical propulsion mechanisms, one induced by bubble production and burst and the other induced by surface tension gradient, were applied and compared across all the SPMs. The enzyme catalase and its substrate hydrogen peroxide were used for driving the SPMs through catalytic reaction and production of bubbles (henceforth called “bubble SPMs”). The surfactant poly (ethylene glycol) (MW = 400) or PEG<sub>400</sub>, which is capable of lowering surface tension, was used for driving the SPMs through surface tension gradient or Marangoni effect (henceforth called “Marangoni SPMs”). The schematic illustration in Fig. 1 shows the propulsion mechanism of bubble and Marangoni SPMs by taking the “1-arm” SPM from each as examples. In a bubble SPM, the hydrogen peroxide present in the surrounding medium gets decomposed into water and oxygen gas bubbles that eventually burst and produce the thrust at the bulging site. In a Marangoni SPM, the leaching of PEG<sub>400</sub> occurs throughout the SPM body and the bulging site.

Within both propulsion mechanisms, the SPMs were printed in four different geometric shapes, as shown in Fig. 2, for comparing the effect of geometry on the propulsion behaviour and trajectories. The length and width of the printed SPMs were approximately  $1.25 \times 0.3$  mm for the main body as measured from the optical micrographs using ImageJ. The main body of 1-arm and 2-arm SPMs were straight lines. In 1-arm bubble SPM, the enzyme was positioned on the side of one end. In 2-arm bubble SPM, the enzyme was located on the alternate sides of the two ends. In 3-arm and 4-arm bubble SPMs, the enzyme was positioned on the same side of the ends of all the arms in order to give directionality during propulsion. In Marangoni SPMs, the design was kept consis-

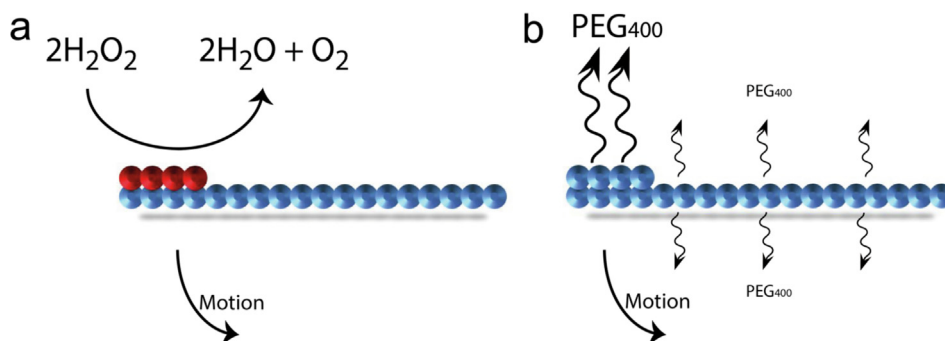


**Fig. 1.** Illustration of the two types of propulsion mechanisms analysed in this study. (a) Bubble propulsion, which is a physical mechanism caused by the thrust produced from the bursting oxygen bubbles. It shows the catalytic breakdown of hydrogen peroxide into water and oxygen by catalase embedded in the SPM's scaffold at desired location (shown in red). (b) Surface tension driven propulsion, also known as Marangoni effect, originating from the concentration gradient caused by the continuous leaching of a surface-active agent, which, in this case, is PEG<sub>400</sub>. (For interpretation of the references to colour in this figure legend, the reader is referred to the web version of this article.)

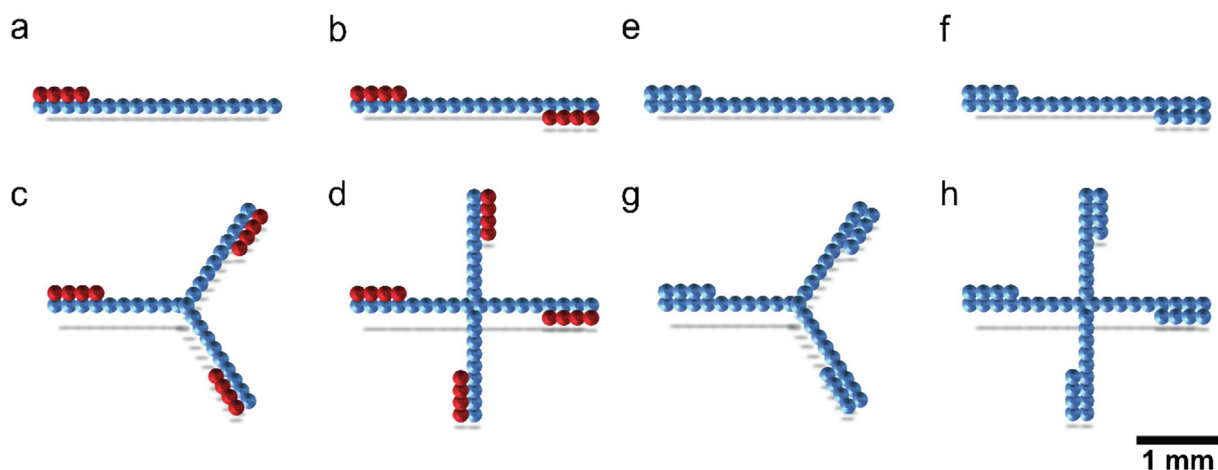


**Fig. 2.** Computer generated illustration of the four geometrical designs of the catalytically driven and surface tension driven SPMs as observed through the Microsoft Excel spreadsheet graph plots. The blue and red colours represent the main body and the catalase positions of the bubble SPMs named as (a) 1-arm, (b) 2-arm, (c) 3-arm, and (d) 4-arm. In the Marangoni SPMs, the whole body of SPMs is uniform in composition and named similarly as (e) 1-arm, (f) 2-arm, (g) 3-arm, and (h) 4-arm. The design of the bulging regions or arms at the tip of the SPM bodies also provides asymmetry to the mass distribution, thus favouring rotational motion. (For interpretation of the references to colour in this figure legend, the reader is referred to the web version of this article.)

tent and similar to the bubble SPMs to allow comparison of the observed motion. Therefore, same geometry was used except that the composition at the bulging regions or the “arms” was kept the same as the rest of the body as there was no addition of any enzyme. In addition, computational fluid dynamics simulations based on the experimental data were performed to illustrate how effective each geometry and mechanism would be at generating fluid motion within a 96-well microwell. The motivation for this assessment is to evaluate a possible application for these devices to overcome current diffusive transport limitations observed in biological assays [43].

## 2. Experimental methods

### 2.1. Materials

*Bombyx mori* silkworm cocoons were obtained from State Key Laboratory of Silkworm Genome Biology and Biological Science Research Centre, Southwest University, China. Catalase enzyme derived from bovine liver, hydrogen peroxide, PEG<sub>400</sub> and all other

chemicals were commercially obtained from Sigma Aldrich, unless otherwise stated, and were of analytical grade.

### 2.2. Fabrication of SPMs by 3D inkjet printing

The regenerated silk fibroin (RSF) solution was prepared using a previously described procedure [27]. The concentrations of RSF and PEG<sub>400</sub> in the fibroin ink (ink 1) were kept at 40 mg/mL and 15 mg/mL, respectively. Additionally, for printing the catalytic arm sites of the bubble SPMs, catalase (catalytic activity > 20,000 units/mg) at 5 mg/mL was mixed in fibroin ink to formulate catalytic fibroin ink (ink 2). Coomassie brilliant blue (0.05 mg/mL) was mixed in methanol to prepare the curing ink (ink 3). The contrasting blue colour ensured better visibility of the SPMs during propulsion and tracking. The three inks were loaded in three separate channels fitted with three separate jetting devices for printing. Each channel was maintained at appropriate jetting parameters, such as voltage and frequency, to ensure good and stable droplet formations. The inks were printed in the following different stages – stage 1: printing of Ink 1 (main body); stage 2: printing of Ink 3 (curing ink); stage 3: printing of Ink 2 (catalytic ink for arm sites)

or Ink 1 (Marangoni SPMs); stage 4: printing of Ink 3 (curing ink); stage 5: repeat Stages 1–4 as required for the desired number of layers (e.g., 100).

### 2.3. Characterization of SPMs

The SPMs were characterized using optical microscopy and scanning electron microscopy (SEM). For acquiring optical micrographs, freshly fabricated SPMs were imaged. For SEM, images were taken separately with both unused (pre-propulsion) and used (post-propulsion) SPM samples. Unused and used SPMs were removed from the silicon wafer and from the propulsion medium, respectively, and carefully placed onto 10 mm wide carbon sticky pads mounted on aluminium SEM stubs. The samples were then dried in a drying oven for 10 min at 60 °C. The stubs with dried samples were loaded onto the sputter coater stage and 50–100 nm of gold was sputter coated onto the samples using argon plasma at 0.05 Torr, thus ensuring a homogeneous gold coating on the sample SPM surface. Afterwards, the stubs with gold-coated samples were loaded into the SEM (Inspect F, FEI) and imaged at 5.0 kV.

### 2.4. SPM propulsion

The SPMs were propelled under room temperature ( $\sim 20$  °C) at the air/water interface. All the experiments were carried out with the well-plates and Petri dishes kept in a thermally-insulated transparent plastic box inside which the ambient temperature was continually monitored and kept constant. For bubble SPM propulsion, the silicon wafer slide with imprinted SPMs was dipped in water for a few minutes to remove the SPMs off the wafer surface and to wash away PEG<sub>400</sub>. A glass Petri dish was rinsed with deionised water, wiped clean, and filled with 10 mL of 5 % w/v H<sub>2</sub>O<sub>2</sub> solution. A washed SPM was then picked up carefully on the tip of a syringe needle and placed on H<sub>2</sub>O<sub>2</sub> solution in the centre of the Petri dish. Eventually, the catalase in the SPM instantly started to catalyse the breakdown of hydrogen peroxide into water and oxygen, causing bubble formation around the arm part of the SPM. The bursting of oxygen bubbles provided force to the SPM which started propelling with circular or rotating motion. The Marangoni SPMs, on the other hand, were taken off the silicon wafer directly with the help of a sharp needle and placed on the surface of deionised water for carrying out the surface tension driven propulsion. The 12-well plate with 23 mm well diameter was selected for propelling Marangoni SPMs to ensure their localization within the camera frame. In case of bubble SPMs, 90 mm Petri dish was chosen to make sure that enough H<sub>2</sub>O<sub>2</sub> was present so that it didn't become a reaction-rate limiting factor. Additionally, as bubble SPM propulsion was much slower than Marangoni SPM propulsion, no bubble SPM propelled out of the video frame.

### 2.5. Propulsion data acquisition

The bottom of the Petri dish or 12-well plate was lit up with a cool-white LED light-source (AGPtek Lightpad) and a high speed PixeLink™ CCD colour camera (model: PL-D732CU-T), fitted with Navitar™ macro zoom lens (1–60135 zoom tube lens with 1–6010 camera coupler attachment), was used to capture and record the SPM propulsions, which were saved as AVI files. A total of 12,000 frames were captured per video per SPM at the rate of 100 frames per second, giving a total length of 120 s per video. After recording, ImageJ was used to generate image sequence from the video frames for all the SPMs.

### 2.6. Tracking & trajectory analysis

Automatic tracking was done by importing the video of a propelling SPM into an in-house built LabVIEW tracking programme [5]. In this programme, the coordinates of each SPM were tracked at its two ends frame-by-frame by calculating the linear displacement of the tracking points between two consecutive frames. The programme then analysed the tracking data, yielding the mean instantaneous velocities of both ends of the SPMs. The tracking programme calculated instantaneous velocities in each frame by locating an SPM's spatial positions in two consecutive frames, then calculating the SPM's spatial displacement between the frames, and then dividing the displacement by the time difference between the two frames (frame rate). In brief, the instantaneous velocity was calculated as SPM displacement divided by the time taken for displacement between two consecutive video frames. The values obtained for each frame were then used for determining the velocity decay of SPMs over time. After tracking was finished, the data was automatically compiled and exported in a Microsoft Excel file.

For tracking the motion of the SPMs, two extreme points, as indicated by green 'X' symbol in Fig. 3, were manually selected on each SPM after importing their propulsion videos in the LabVIEW tracking software. These points continuously tracked the SPM displacement frame-by-frame and traced the overall path as red and green lines as seen in the time-lapse images in Figs. 6 and 7. The linear displacement shown in purple arrow helped in automated calculation of the instantaneous velocity by dividing the displacement by time taken between two frames. The change in angle of orientation  $\phi$  over time was measured to obtain data on rotations per minute.

### 2.7. RPM counter

An in-house built LabVIEW programme was used to accurately count the number of rotations and calculate RPM. The programme imported and read the Excel files consisting of the instantaneous angles of orientation obtained from the tracking data and then calculated the RPM by counting the repeats, or the peaks / valleys as seen in a graphical data, in the angle of orientation of the SPMs. The rate of change of RPM was calculated by finding the times taken by angles of orientation to complete the consecutive cycles of 360°

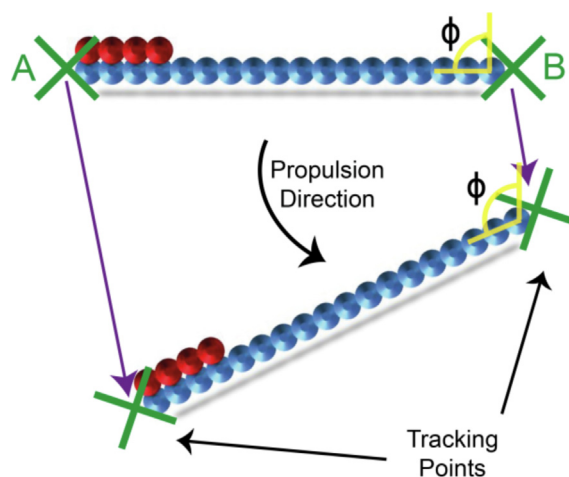


**Fig. 3.** Schematic representation of SPM tracking over two consecutive frames. 'A' and 'B' indicate tracking points and C indicates the centre of mass. The symbol  $\phi$  indicates the angle of orientation. SPM trajectory direction is indicated by the curved black arrow.

and then plotting the obtained values over the 120 s of observation time period.

### 2.8. Simulation

Computational Fluid Dynamics (CFD) simulations of the experimental SPM's ability to induce fluid flow in 96-well plate microwells were performed using COMSOL (Comsol Inc.) software. The SPMs were simulated while rotating in the centre of a water filled well (diameter = 5 mm, depth = 11 mm) at 20 °C with a constant rotational rate that matched the mean experimentally observed RPM values. The SPM dimensions matched the experimental sizes, with geometry simplified to smooth sided 3D shapes. All the liquid–solid boundaries were assumed to be non-slip, and the top surface was modelled as an air–water interface. The system was found to be laminar, based on calculating the relevant mixing Reynolds number, and therefore, simulation was performed excluding turbulence. Frozen SPM solutions are presented in the results, which show the predicted steady state behaviour for the system under these conditions. Time resolved simulations were also performed, which showed consistency with the output from the frozen SPM solutions, and did not reveal a significant dependency on the “ramp-up” profiles of the rotary motion. Note that these simulations only consider the flows induced by the rotating SPMs, they do not consider any additional flow effects that the propulsion mechanisms themselves may introduce, for example bubble SPMs may be expected to produce additional perturbations as gas bubbles are released from their surface.

### 2.9. Statistics

The instantaneous velocities and angular or rotational angles ( $\Phi$ ) of the propelling SPMs were generated once every 0.01 s, which was the time gap between two consecutive video frames. This gave a total of 12,000 data points for instantaneous velocity and angular position for a 120 s long video. These instantaneous velocities and angular positions or angles of orientation ( $\Phi$ ) were then plotted against time ( $t$ ) to generate the instantaneous velocity decay curve and angular velocity decay curve of each SPM. Next, the change in angular orientation ( $\delta\Phi$ ) between two consecutive video frames was plotted against the change in time ( $\delta t$ ) between two consecutive video frames. This generated the graph showing rate of change of angular velocity or RPM (deceleration or acceleration) of each SPM. All the graphs were plotted in Origin™.

## 3. Results

The optical micrographs of freshly printed bubble and Marangoni SPMs are shown in Fig. 4. In the bubble SPMs, the rectangular red regions show the bulging region or arm where fibroin is doped with catalase. In the Marangoni SPMs, the rectangular red region shows the bulging region or arm which ensures that the design of SPMs remains consistent and asymmetrical across the bubble and Marangoni propulsions. Several satellite droplets are also seen deposited around the SPMs which do not remain after the SPMs are removed from the silicon wafer substrate.

High magnification images of the SPMs were obtained using SEM to analyse the topography of bubble and Marangoni SPMs both before and after their propulsion. As evident in Fig. 5 (a–b), the bulging region or arm of the bubble SPM showed smooth texture before propulsion and a rough and punctured texture after propulsion. The punctures indicate the site of catalytic reaction and oxygen bubble formation. On the other hand, the bulging region or arm of the Marangoni SPMs showed visibly smooth texture both before and after propulsion as shown in Fig. 5 (c–d). This is because of the smooth and continuous leaching of PEG<sub>400</sub> molecules which are significantly smaller than the oxygen bubble produced vigorously at certain weak points on the bubble SPM surface.

Selected video frames from the propulsion of bubble and Marangoni SPMs are shown in Figs. 6 and 7. Each bubble SPM produced consistent rotation, showing that the location of the enzyme patches has achieved the desired effect for each design. The bubble SPMs were not, however, showing pure rotations, and also made some translations over the period of observation, moving around 1 cm from their initial position. The overall bubble SPM trajectories are angular for all four geometric shapes and show jerky motion. Considering the Marangoni SPMs, the 1- and 2- arm SPMs have striking trajectories, producing smooth, larger radius circles compared to the bubble SPMs. The 1-arm SPM clearly interacted with the container boundary, causing the circling trajectory to follow the edge of the container. Overall, much larger translations occurred than those for the bubble SPM (around 10 cm travelled in the same time period). The 2-arm SPM largely moved within the centre of the container, but occasionally reached the edge, and also showed more variability in the radius of the circling behaviour. In contrast, the 3- and 4- arm SPMs were somewhat harder to categorise, but shared features of wide radius circling, as well as

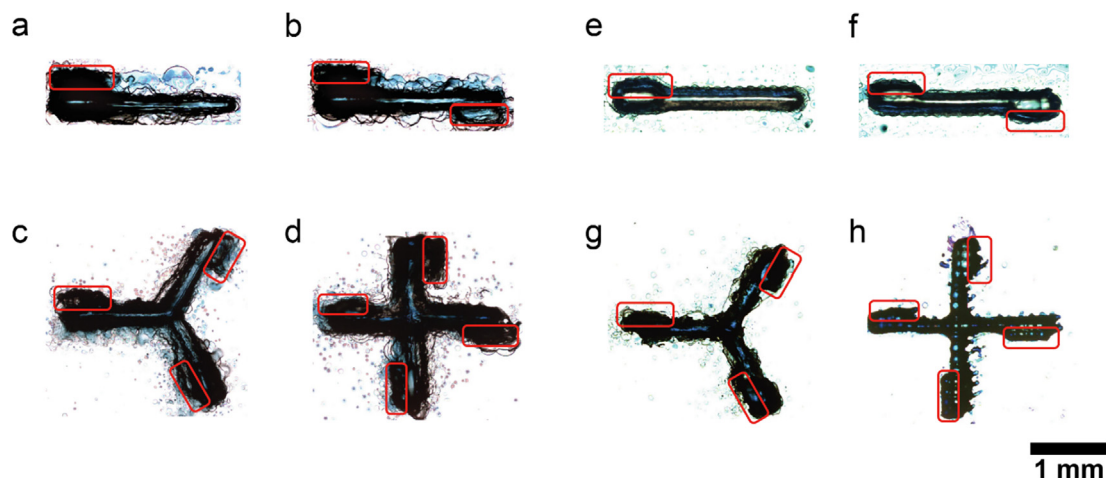


**Fig. 4.** Optical micrographs of freshly fabricated bubble SPMs with catalytically active (a) 1-arm, (b) 2-arm, (c) 3-arm, and (d) 4-arm regions shown in red box. Optical micrographs of freshly fabricated Marangoni SPMs with (e) 1-arm, (f) 2-arm, (g) 3-arm, and (h) 4-arm regions shown in red box. (For interpretation of the references to colour in this figure legend, the reader is referred to the web version of this article.)

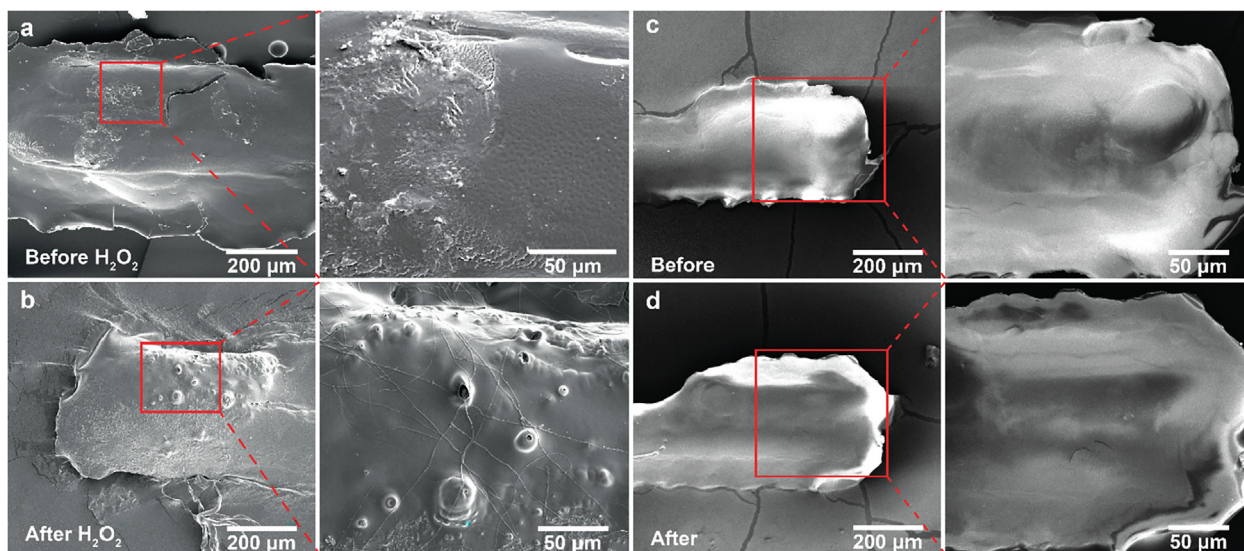


**Fig. 5.** (a – b) SEM images of the main body and catalase arm part of a bubble SPM before (a) and after (b) exposure to 5% w/v H<sub>2</sub>O<sub>2</sub> fuel solution. Pores can be clearly seen on the arm surface in the SEM images of the SPMs originating from the oxygen bubble release. Images on the right are enlargements of the red boxed regions. (c – d) SEM images of the main body and arm of a Marangoni SPM before (c) and after (d) exposure to DI water. No significant differences are observed in the morphology or surface features between the pre-propulsion and post-propulsion images. (For interpretation of the references to colour in this figure legend, the reader is referred to the web version of this article.)

interactions with the boundary that occasionally led to fleeting almost linear motion, and some edge following. In practice, over the observation of many Marangoni SPMs of each design, similar features were seen, but with a high degree of variability, so that the overall behaviour is best described as variable radius circling, with appreciable translations also occurring and evidence of interaction with the container boundaries. In order to systematise the differences between the designs and mechanisms, quantitative analysis is required. A simple metric is the instantaneous velocity ( $v_{inst}$ ), which will reflect both the rotational and translational motion magnitude, and allows comparison and temporal analysis. Fig. 8 compares the instantaneous velocity decays of one representative SPM belonging to each of the four geometric shapes and each of the two propulsion mechanisms. All four bubble SPMs showed similar behaviour, with fluctuations, but a clear trend of reducing velocity with residual motion still occurring at the end of the tracking period. In contrast, the Marangoni SPMs showed smoother, but still decaying trends in instantaneous velocity. Despite the magnitude of instantaneous velocity produced by the Marangoni SPMs starting at a factor of 10 higher than for the bubble SPMs, by the end of the observation period, the Marangoni SPM speed had decayed to a similar, or, in some examples, lower values compared to the bubble equivalents.

Instantaneous velocity provides an overall comparison of motion producing ability, however, as we are interested in rotary motion, considering the rate of change of orientation with time is also instructive as shown in Fig. 9. With bubble propulsion, the 3- and 4- arm SPMs showed relatively more periodic propulsion in comparison to the 1- and 2- arm SPMs as shown in Fig. 9 (a). This could be due to the higher number of catalase-doped sites in 3- and 4- arm SPMs ensuring that more bubbles were regularly formed and available for propelling the SPM, leading to fewer periods of rest when no bubble burst. The high temporal resolution graph for the orientation changes of the 1-arm bubble SPM clearly shows that motion is proceeding via angle jumps then rests which is typical of bubble propulsion as shown in Fig. 9 (c). It is clearly evident that the Marangoni SPMs undergo a rapid change in angle of orientation which is several times faster than that of the bubble SPMs as shown in Fig. 9 (b). In contrast, the high temporal resolu-

tion data for the equivalent 1-arm Marangoni propulsion SPM shows very smooth, continuous rotation, reflecting the quite different propulsion mechanism as shown in Fig. 9 (d). The 1- and 2-arm SPMs showed longer sustained rapid rotation in comparison to the 3- and 4- arm SPMs. This could be attributed to the more rapid release of surface tension lowering agent as the number of arms increase leading to more rapid loss of the required motion producing gradient.

As another comparator, the mean RPM of each type of SPM for both propulsion mechanisms, calculated from the angle of orientation data is shown in Fig. 10 (a). Overall, the RPMs of Marangoni SPMs were found to be around 10-times more than those of the bubble SPMs. Within Marangoni propulsion, the 1- and 2- arm SPMs showed much higher RPM averaged throughout the 120 s of observation time compared to the 3- and 4- arm ones, as discussed above. The different bubble SPMs showed similar mean RPM values.

From the data on angle of orientation and mean RPM, it is difficult to decipher whether the RPM of the SPMs decelerated evenly or showed high degree of fluctuations throughout the observation period of 120 s. Accordingly, the rate of change of RPM of representative SPMs were also plotted against time as shown in Fig. 10 (b). Similar to the data in angle of orientation and mean RPM, the Marangoni SPMs showed around 10-times higher degree of fluctuation in the rate of change or deceleration of RPM. However, the 1-arm Marangoni SPM showed the least fluctuation as observed in its amplitude. In summary, both SPM types produce rotations, as intended by their design, however the resulting trajectories, velocities and rotational behaviour differ considerably, showing that mechanism plays a major role in determining the behaviour.

Following this comprehensive analysis of the experimental behaviour, the potential to exploit these SPMs to enhance mixing in smaller fluid volumes is also assessed. Attempts to measure the mixing efficiency of current SPMs in smaller sized containers is challenging due to them sticking to container walls. However, envisaging that this issue can be overcome, we instead consider possible stirring effects using computational fluid dynamics (CFD) simulations. One impactful application for SPMs would be to increase mass transport in medical diagnosis assays [43], which

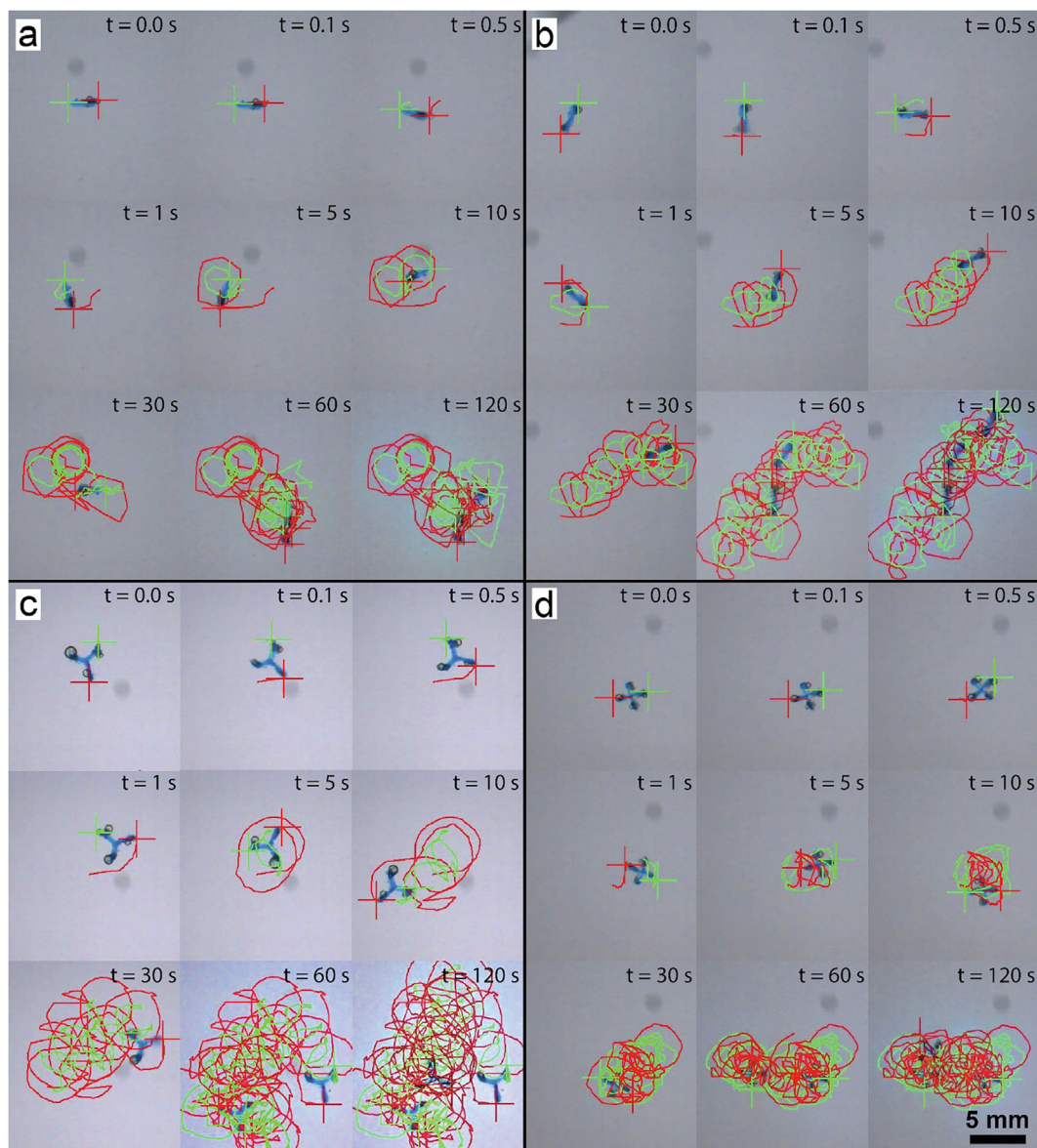


**Fig. 6.** Representative video frames of bubble SPMs propelling in 5%  $\text{H}_2\text{O}_2$  fuel solution showing the trajectory over time at selected timestamps up to 120 s. (a) 1-arm, (b) 2-arm, (c) 3-arm, and (d) 4-arm.

can be limited by the diffusion rate of analytes to surface bound detection chemistry. Consequently, given the ubiquity of 96 well plates in diagnostics, we have simulated the fluid velocity and streamlines for each SPM studied here rotating within this geometry. Fig. 11 shows a comparison of the results for the bubble SPMs. It is clear that each SPM perturbs the fluid and, reflecting the similar RPM values, the maximum fluid flow velocities induced are similar for the 1–3 arm SPMs, with a slight reduction seen for the 4-arm SPM. When considering the 2D flow velocity profiles, it is clear that the 3-arm SPM produces the most extensive perturbations to the fluid, both in the XY and XZ planes. The ability to rotate this 3 “armed” SPM without a reduction in RPM compared to 1 and 2 arm designs consequently maximises fluid velocity within the microwell. The streamlines provide additional insights: as the number of arms in the SPM geometry increases, streamlines increasingly indicate rotary motion occurring around the central axis of the well, and extending to the lower surface (11 mm below the SPM). For SPMs with fewer “arms” the extension of the mixing effect throughout the well is reduced, and the tendency for fluid rotations that are perpendicular to the central axis of the well

are also seen. Fig. 12 shows the simulations for Marangoni SPMs: the maximum fluid velocity is higher (1.6 cm/s compared to 0.25 cm/s for bubble SPMs) reflecting the higher RPM achievable for Marangoni SPMs. Congruence with the bubble SPM simulations is shown when considering the streamlines, with 3- and 4- arm SPMs encouraging rotation about the microwell axis, extending throughout the fluid volume. However, the drop in RPM for 3- and 4- arm SPMs is also apparent in the reduced magnitude and extent of fluid velocity increases induced by these SPMs. Consequently, utilising the 3- and 4- arm geometries which are efficient at stirring sacrifices some of the Marangoni effect’s potential to generate large fluid velocities. Despite this, the fluid velocities induced by these 3- and 4- arm Marangoni SPMs remain approximately double that of the equivalent bubble SPMs.

#### 4. Discussion

During propulsion, all SPM positions remained parallel to the fluid surface and as the SPMs were large and millimetre-scale, their

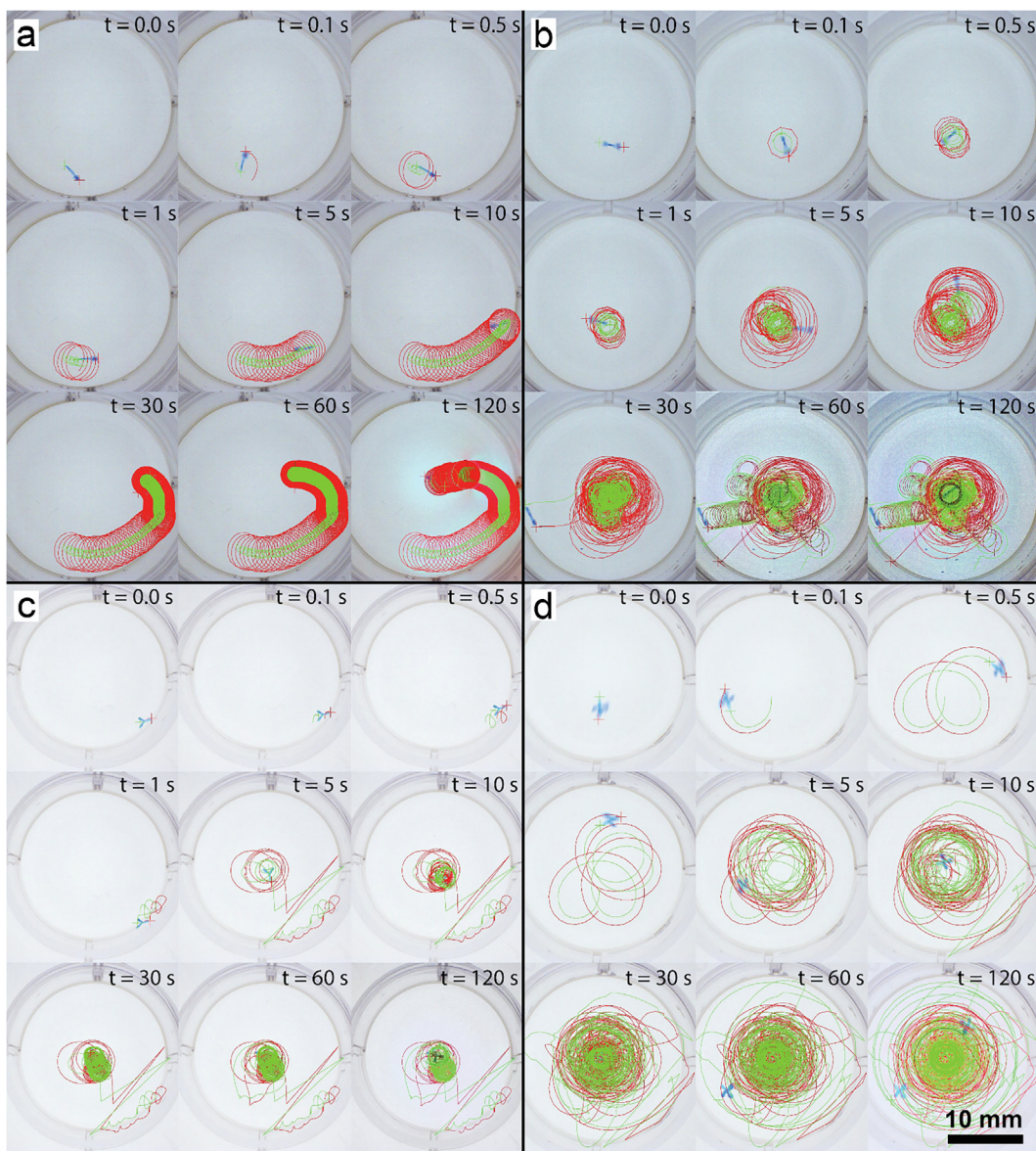


**Fig. 7.** Representative video frames of Marangoni SPMs propelling in DI-water showing the trajectory over time at selected timestamps up to 120 s. (a) 1-arm, (b) 2-arm, (c) 3-arm, and (d) 4-arm.

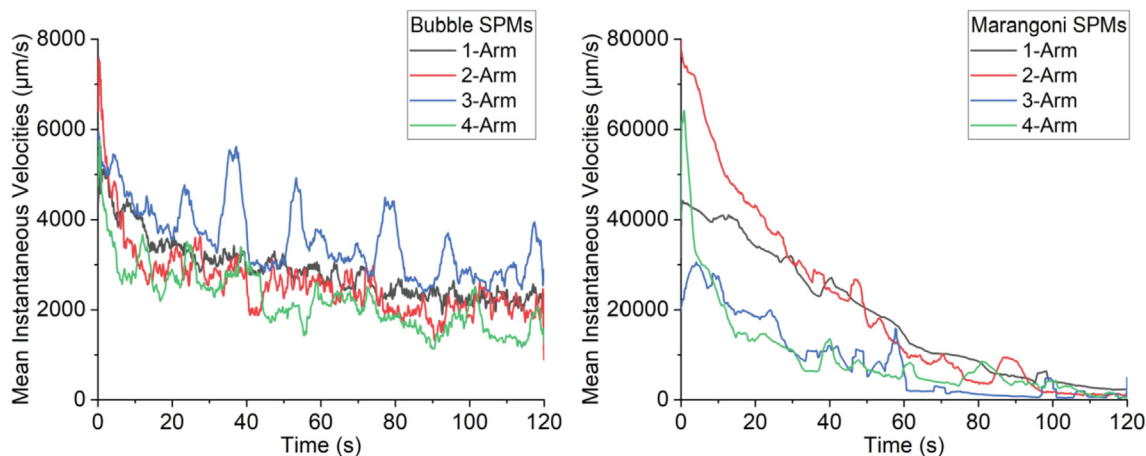


**Fig. 8.** Instantaneous velocity deceleration, as measured at one of the two ends of a representative SPM, plotted for the four bubble SPMs and the four Marangoni SPMs.

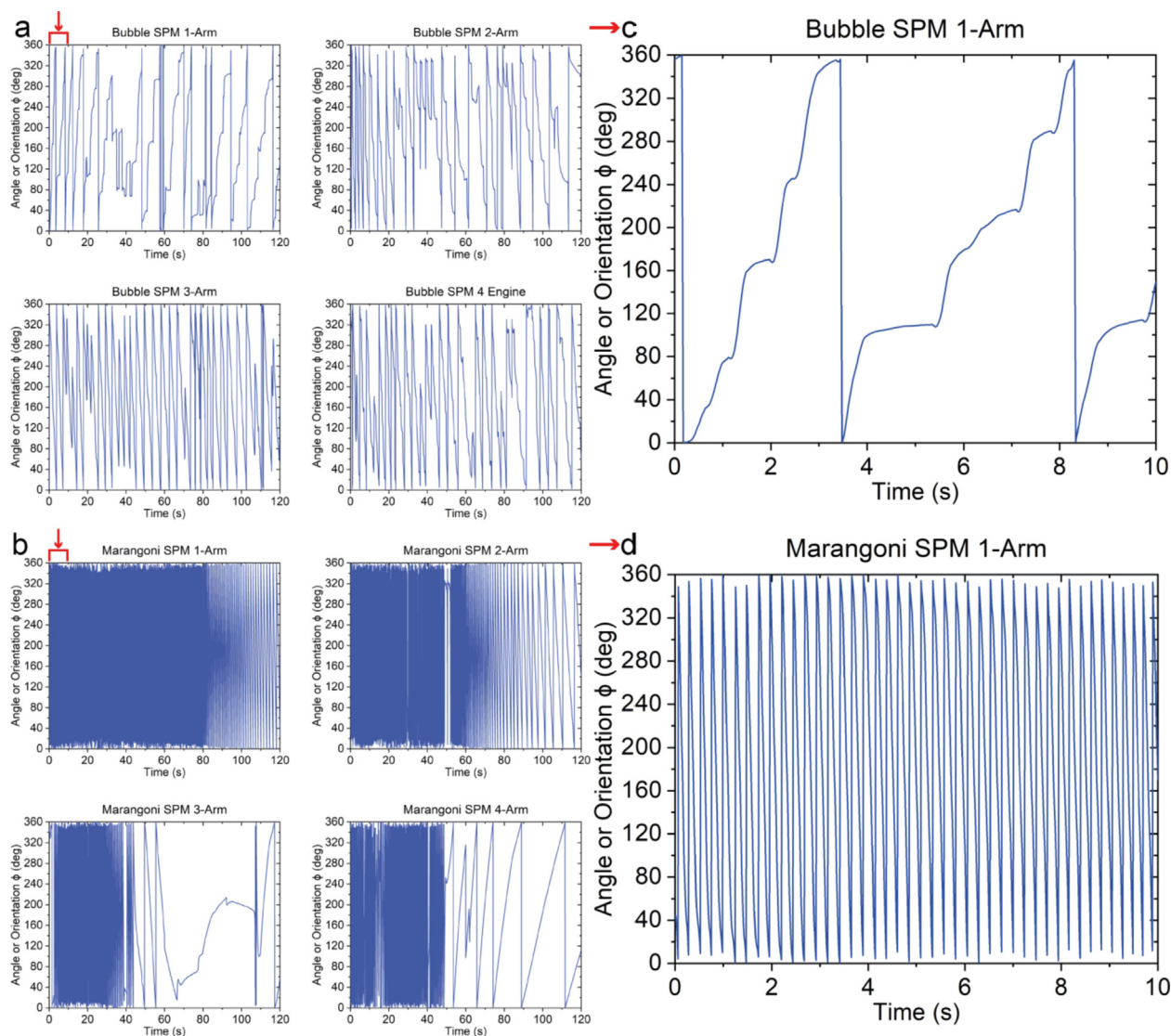


**Fig. 9.** Angle of orientation of representative (a) bubble SPMs and (b) Marangoni SPMs over the propulsion period of 120 s. The first 10 s of propulsion data in one graph each from (a) and (b) are selected (red bracket with arrow) and magnified in (c) and (d), respectively (red arrows). (For interpretation of the references to colour in this figure legend, the reader is referred to the web version of this article.)

propulsion was not affected by Brownian motion, which otherwise affects the propulsion of nano- and micron- scale particles.

Comparing propulsion mechanisms, in bubble SPMs, the bulging regions or arms contained the enzyme catalase causing the catalytic decomposition of hydrogen peroxide and oxygen bubble production in these regions. The bubbles, on bursting, created a thrust and pushed the SPMs in the opposite direction leading to propulsion. Additionally, the PEG<sub>400</sub> made the SPM structure more porous after getting washed out, allowing easier interaction of catalase and H<sub>2</sub>O<sub>2</sub> and bursting of bubbles [5]. In Marangoni SPMs a PEG<sub>400</sub> concentration gradient caused surface tension gradient driven propulsion. As previous studies have shown, in the self-propelling systems at a fluid interface, there can be two mechanisms, concentration and thermal Marangoni flows, which determine the net displacement of the motors [44,45]. However, uncovering and segregating the two mechanisms at this level of detail was not part of the remit of this study. As the self-propelling motor system is at millimetre scale, and each self-propelling motor was placed in a Petri dish with 10 mL water, we don't expect a noticeable thermal effect. Therefore, it is not a crucial issue that would alter any of the conclusions or change

the novel and impactful elements of our report. However, a full mechanistic study could well form the basis for a future study.

The bulging end of arms of SPMs was kept the same for both the propulsion mechanisms and were designed to provide an asymmetry in shape with an intent to cause rotation as the primary form of propulsion when the SPMs were pushed by either bubbles or surface tension gradient. Each propulsion mechanism exploited different features of the uneven mass distribution. For bubble SPMs, the driven rotations reflected the localisation of the "arms", arranged on the same side of each arm to statistically deliver cooperative bubble release thrust encouraging rotation. Whereas for Marangoni SPM the bulges broke the otherwise symmetrical opportunity for PEG<sub>400</sub> leaching, also resulting in consistent rotary motion. It is possible that spontaneous symmetry breaking would allow purely symmetrical designs to undergo similar behaviour in the case of Marangoni SPM, while it is likely that symmetrical bubble SPM designs would not display consistent rotations as bubble release from either side of each arm would remain equally likely.

For bubble SPMs, bubbling was not smooth and caused uneven periods of rest and motion throughout the propulsion. The irregular pattern of bursting of bubbles also posed a problem in providing

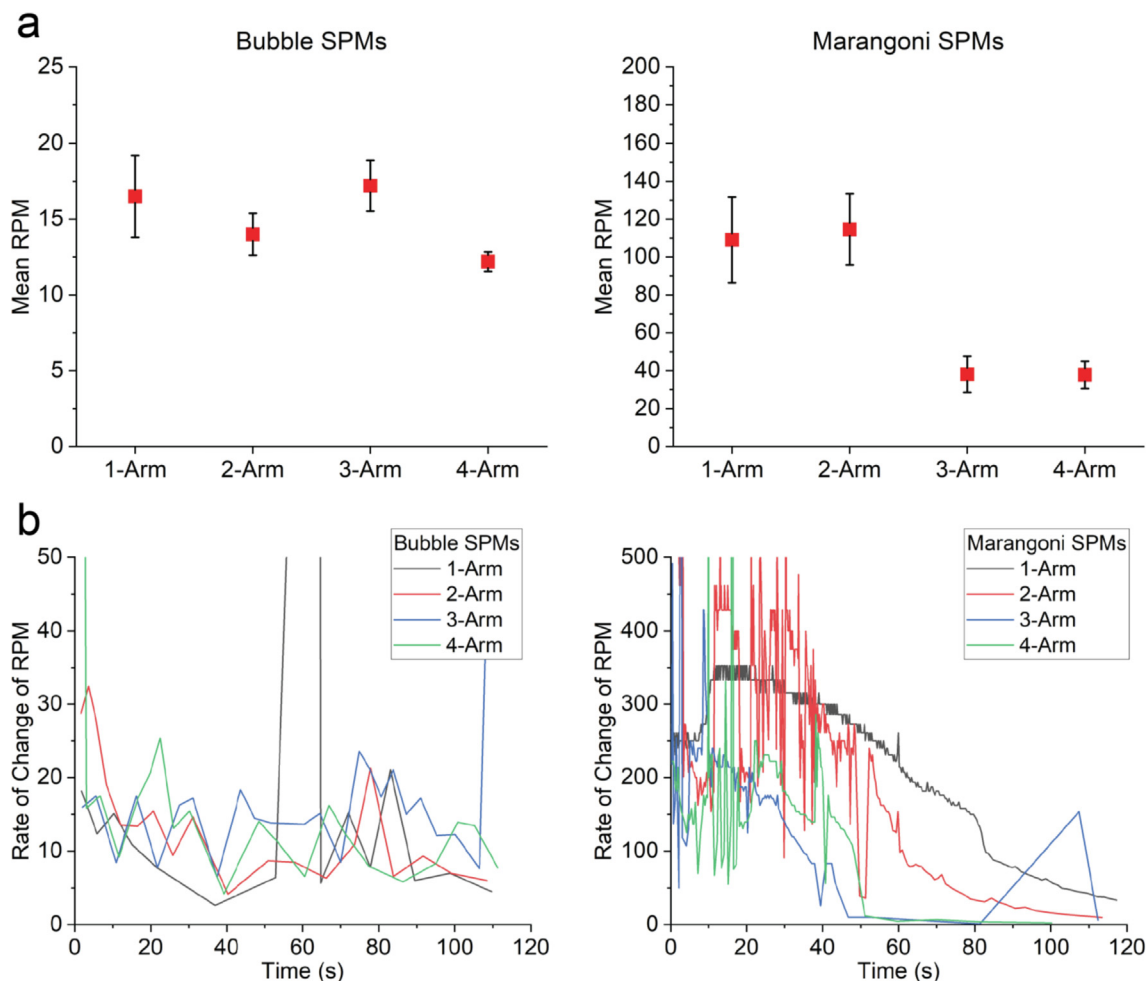


**Fig. 10.** (a) Mean RPM of five samples each of bubble and Marangoni SPMs with standard deviations. (b) Fluctuation in RPM of bubble and Marangoni SPMs over 120 s of observation time period. One representative sample from each of the four geometries is shown here.

accuracy in predicting the motion. In Marangoni SPMs the continuous release of PEG<sub>400</sub> and time invariant mechanism resulted in smoother motion and deceleration. Though around 10-times slower, instantaneous velocities were measured at same time intervals, the propulsions of bubble SPMs lasted as long as those of the Marangoni SPMs, and also surpassed the case of 3-arm and 4-arm SPMs after the 40–50 s mark. This was because the decomposition of hydrogen peroxide by catalase is a first-order reaction with respect to either of the reactants and is affected only by the concentration of hydrogen peroxide, which is slow to deplete given the relatively small reactive areas on the devices. From the image sequence of the video frames, it is clear that the spatial extent of the fluid interface explored over time was much larger in all Marangoni SPMs in comparison to their bubble counterparts.

Considering the overall performance for each shape, the 1-arm surface tension driven Marangoni SPM showed the most predictable and consistent propulsion throughout the observation period. However, in the CFD simulations for mixing, the general trend was found to be in favour of the higher number of arms as they caused agitation throughout the fluid volume as traced and presented by the fluid flow streamlines. Combining the experimental and simulation results thus presented an interesting observation and necessitates a choice of SPM to reflect the specific application and its requirement, that is, slow and steady agitation over longer time periods versus quick and vigorous agitation. However, Marangoni SPMs do appear to have several key advantages

for micro-stirring including faster propulsion velocities, smoother velocity decay, and usability in virtually any neutral fluid medium with a compatible surface tension that can be lowered by additive release. Unpredictable and slower motion and the limitation in fluid choice in bubble propulsion appear as drawbacks for bubble SPMs, although partially offset by the potential for longer lasting rotations. Bubble SPM longevity may be further improved from that reported here with additional refinement of the enzyme attachment strategies and operation in buffered, pH-controlled solutions at biological temperatures, which may be appropriate for some applications.

### 5. Conclusion

In this study, two propulsion mechanisms were compared in four geometric shapes of millimetre-scale self-propelled motors fabricated from silk fibroin using 3D inkjet printing technology. Up to 120 s of propulsion and tracking data were obtained for each sample. The data were obtained from the mean of values of 5 samples for each type of SPM, whereas, instantaneous velocity decay over time and angular velocity or RPM fluctuation and deceleration over time were shown for one representative SPM from each sample type. The results obtained in this study reveals that the surface tension driven propulsion of SPMs with simple geometry showed smooth deceleration and sustained propulsion for extended periods of time and it is, therefore, most suitable for potential micro-

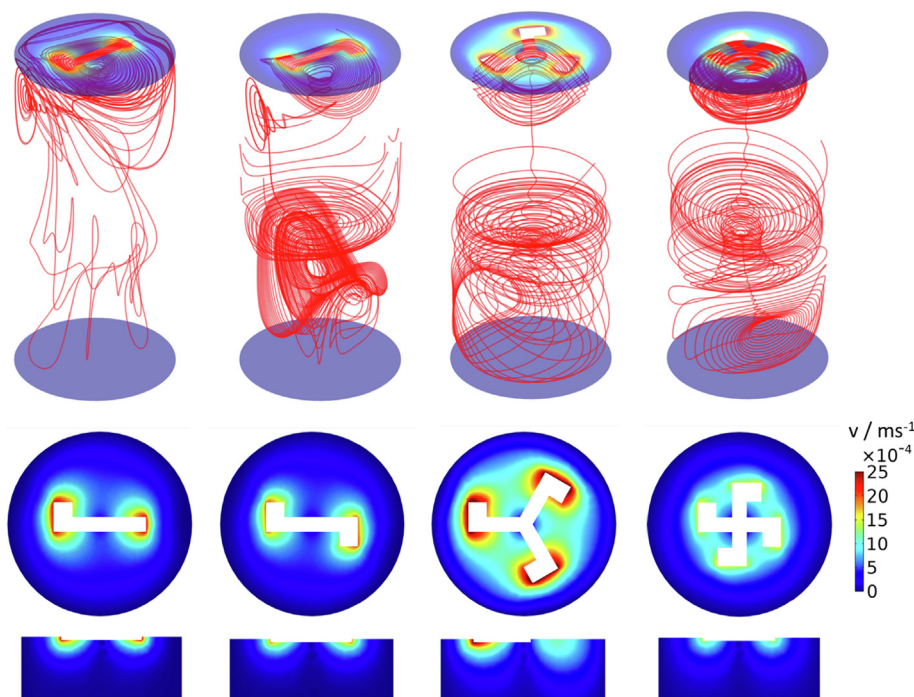


**Fig. 11.** Simulated steady state flow velocity and streamlines for 1–4 arm bubble SPMs (left to right) in a 96 plate microwell (5 mm diameter × 11 mm depth) rotating at the experimentally observed mean RPM. **Top images:** 3D streamline plot superimposed with XY velocity at well top and bottom. **Middle images:** 2D XY velocity profile at surface of microwell. **Lower images:** 2D XZ velocity profile aligned with SPM arm orientation.

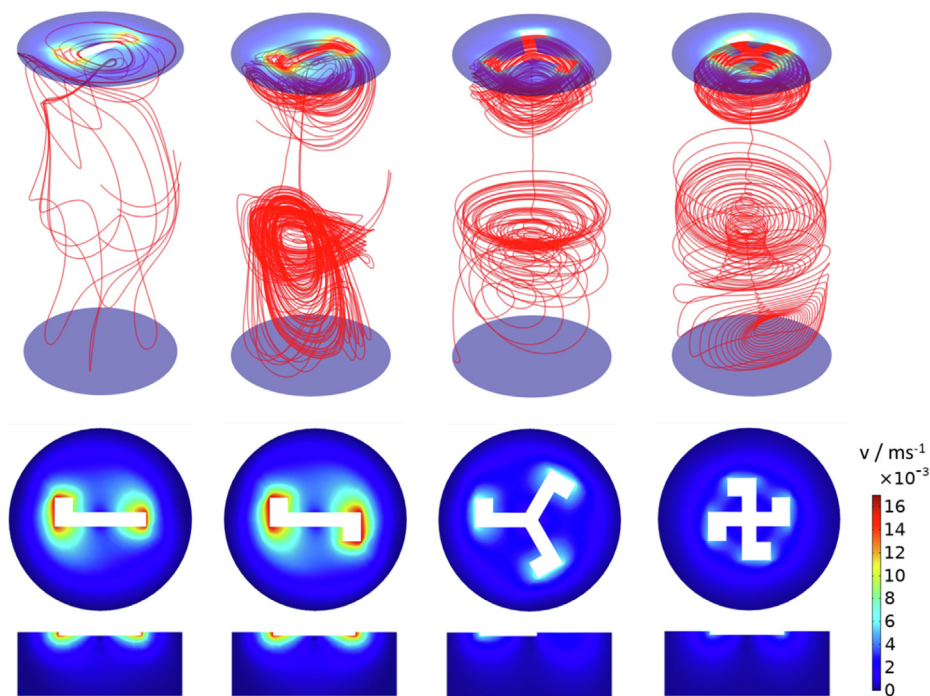


**Fig. 12.** Simulated steady state flow velocity and streamlines for 1–4 arm Marangoni SPMs (Left to right) in a 96 plate microwell (5 mm diameter × 11 mm depth) rotating at the experimentally observed mean RPM. **Top images:** 3D streamline plot superimposed with XY velocity at well top and bottom. **Middle images:** 2D XY velocity profile at surface of microwell. **Lower images:** 2D XZ velocity profile aligned with SPM arm orientation.

stirring applications in biomedical assays. Additionally, surface tension driven particles can be applied in almost any fluid media as long as the leaching surface active agent is chemically neutral to the fluid.

Even though nano and micro scale self-propelled motors or particles have been extensively studied, very little research has been

conducted on macroscopic millimetre-sized SPMs [29]. Our study is thus an important addition to the field of SPM research and explores the potential applications, such as enhancement of biomedical assay sensitivity, especially those ones where slow-diffusing analytes are dominant causing their scarcity near the assay reaction surfaces [43]. In the future, our study can be

repeated with such analytes to establish the importance of SPMs in such cases. Our research can thus lay the foundation for work on macroscopic SPMs so that their applications can increasingly be brought out of the lab towards applications.

#### CRedit authorship contribution statement

**Piyush Kumar:** Conceptualization, Methodology, Software, Validation, Formal analysis, Investigation, Data curation, Writing – original draft, Writing – review & editing, Visualization. **Yi Zhang:** Conceptualization, Methodology, Investigation. **Stephen J. Ebbens:** Conceptualization, Methodology, Software, Validation, Formal analysis, Resources, Writing – review & editing, Supervision, Funding acquisition. **Xiubo Zhao:** Conceptualization, Methodology, Validation, Resources, Writing – review & editing, Supervision, Project administration, Funding acquisition.

#### Declaration of Competing Interest

The authors declare that they have no known competing financial interests or personal relationships that could have appeared to influence the work reported in this paper.

#### Acknowledgements

The authors would like to acknowledge the EPSRC (EP/N007174/1, EP/N023579/1, EP/J002402/1, and EP/N033736/1) for support. The authors would also like to thank Professor Feng Wang and Professor Qingyou Xia of Southwest University, China for providing the silk cocoons.

#### Appendix A. Supplementary material

Supplementary videos 1 to 4 showing bubble propulsion and 5 to 8 showing Marangoni propulsion. Supplementary data to this article can be found online at <https://doi.org/10.1016/j.jcis.2022.05.011>.

#### References

- [1] D.A. Gregory, A.I. Campbell, S.J. Ebbens, Effect of catalyst distribution on spherical bubble swimmer trajectories, *J. Phys. Chem. C* 119 (27) (2015) 15339–15348.
- [2] W.F. Paxton, K.C. Kistler, C.C. Olmeda, A. Sen, S.K. St, Y. Angelo, T.E. Cao, P.E. Mallouk, V.H.C. Lammert, Catalytic nanomotors: autonomous movement of striped nanorods, *J. Am. Chem. Soc.* 126 (41) (2004) 13424–13431.
- [3] W. Gao, X. Feng, A. Pei, Y. Gu, J. Li, J. Wang, Seawater-driven magnesium based Janus micromotors for environmental remediation, *Nanoscale* 5 (11) (2013) 4696–4700.
- [4] J. Li, V.V. Singh, S. Sattayasamitsathit, J. Orozco, K. Kaufmann, R. Dong, W. Gao, B. Jurado-Sanchez, Y. Fedorak, J. Wang, Water-driven micromotors for rapid photocatalytic degradation of biological and chemical warfare agents, *ACS Nano* 8 (11) (2014) 11118–11125.
- [5] D.A. Gregory, Y.u. Zhang, P.J. Smith, X. Zhao, S.J. Ebbens, Reactive inkjet printing of biocompatible enzyme powered silk micro-rockets, *Small* 12 (30) (2016) 4048–4055.
- [6] R.F. Ismagilov, A. Schwartz, N. Bowden, G.M. Whitesides, Autonomous movement and self-assembly, *Angew. Chem. Int. Ed.* 41 (4) (2002) 652–654.
- [7] V. Pimienta, C. Antoine, Self-propulsion on liquid surfaces, *Curr. Opin. Colloid Interface Sci.* 19 (4) (2014) 290–299.
- [8] P. Kumar, A. Legge, D.A. Gregory, A. Nichols, H. Jensen, S.J. Ebbens, X. Zhao, 3D printable self-propelling sensors for the assessment of water quality via surface tension, *JCS Open* 5 (2022) 100044.
- [9] M. Xuan, Z. Wu, J. Shao, L. Dai, T. Si, Q. He, Near infrared light-powered janus mesoporous silica nanoparticle motors, *J Am Chem Soc* 138 (20) (2016) 6492–6497.
- [10] V. Garcia-Gradilla, J. Orozco, S. Sattayasamitsathit, F. Soto, F. Kuralay, A. Pourazary, A. Katzenberg, W. Gao, Y. Shen, J. Wang, Functionalized ultrasound-propelled magnetically guided nanomotors: toward practical biomedical applications, *ACS Nano* 7 (10) (2013) 9232–9240.
- [11] T. Li, J. Li, K.I. Morozov, Z. Wu, T. Xu, I. Rozen, A.M. Leshansky, L. Li, J. Wang, Highly efficient freestyle magnetic nanoswimmer, *Nano Lett.* 17 (8) (2017) 5092–5098.
- [12] A. Barbot, D. Decanini, G. Hwang, Controllable roll-to-swim motion transition of helical nanoswimmers, *IEEE/RSJ Int. Conf. Intell. Robots Syst.* 2014 (2014) 4662–4667.
- [13] I. Santiago, F.C. Simmel, Self-propulsion strategies for artificial cell-like compartments, *Nanomaterials* 9 (12) (2019) 1680.
- [14] C. Tomlinson, XLVII. On the motions of camphor on the surface of water, *The London, Edinburgh, and Dublin Philosophical Magazine and Journal of Science* 38(257) (1869) 409–424.
- [15] S. Nakata, Y. Iguchi, S. Ose, M. Kuboyama, T. Ishii, K. Yoshikawa, Self-rotation of a camphor scraping on water: new insight into the old problem, *Langmuir* 13 (16) (1997) 4454–4458.
- [16] D. Boniface, C. Cottin-Bizonne, R. Kervil, C. Ybert, F. Detcheverry, Self-propulsion of symmetric chemically active particles: point-source model and experiments on camphor disks, *Phys. Rev. E* 99 (6–1) (2019) 062605.
- [17] C.N. Baroud, Marangoni Convection, in: D. Li (Ed.), *Encyclopedia of Microfluidics and Nanofluidics*, Springer US, Boston, MA, 2013, pp. 1–8, [https://doi.org/10.1007/978-3-642-27758-0\\_852-4](https://doi.org/10.1007/978-3-642-27758-0_852-4).
- [18] B.E. Rapp, Chapter 20 - Surface Tension, in: B.E. Rapp (Ed.), *Microfluidics: Modelling, Mechanics and Mathematics*, Elsevier, Oxford, 2017, pp. 421–444.
- [19] L. Meggs, The Marangoni Effect: A Fluid Phenom, 2011. [https://www.nasa.gov/mission\\_pages/station/research/news/marangoni.html](https://www.nasa.gov/mission_pages/station/research/news/marangoni.html).
- [20] Y. Zhang, D.A. Gregory, Y. Zhang, P.J. Smith, S.J. Ebbens, X. Zhao, Reactive Inkjet Printing of Functional Silk Stirrers for Enhanced Mixing and Sensing, *Small* 15 (1) (2019) e1804213.
- [21] H. Hu, R.G. Larson, Marangoni effect reverses coffee-ring depositions, *J. Phys. Chem. B* 110 (14) (2006) 7090–7094.
- [22] I. COMSOL, The Marangoni Effect, 2017. <https://www.comsol.com/multiphysics/marangoni-effect>
- [23] K.K. Dey, A. Sen, Chemically propelled molecules and machines, *J. Am. Chem. Soc.* 139 (23) (2017) 7666–7676.
- [24] E.J. Banigan, J.F. Marko, Self-propulsion and interactions of catalytic particles in a chemically active medium, *Phys Rev E* 93 (1) (2016) 012611.
- [25] W.F. Paxton, A. Sen, T.E. Mallouk, Motility of catalytic nanoparticles through self-generated forces, *Chemistry* 11 (22) (2005) 6462–6470.
- [26] S.J. Ebbens, J.R. Howse, Direct observation of the direction of motion for spherical catalytic swimmers, *Langmuir* 27 (20) (2011) 12293–12296.
- [27] D.A. Gregory, P. Kumar, A. Jimenez-Franco, Y. Zhang, Y. Zhang, S.J. Ebbens, X.B. Zhao, Reactive Inkjet Printing and Propulsion Analysis of Silk-based Self-propelled Micro-stirrers, *Jove-J Vis Exp* (146) (2019) e59030.
- [28] M. Guix, S.M. Weiz, O.G. Schmidt, M. Medina-Sánchez, Self-propelled micro/nanoparticle motors, *Part. Part. Syst. Char.* 35 (2) (2018) 1700382.
- [29] G. Zhao, M. Pumera, Macroscopic self-propelled objects, *Chem. –Asian J.* 7 (9) (2012) 1994–2002.
- [30] A. Halder, Y. Sun, Biocompatible propulsion for biomedical micro/nano robotics, *Biosens. Bioelectron.* 139 (2019) 111334.
- [31] N.M. Oliveira, R.L. Reis, J.F. Mano, The potential of liquid marbles for biomedical applications: a critical review, *Adv. Healthcare Mater.* 6 (19) (2017) 1700192.
- [32] L.K.E.A. Abdelmohsen, F. Peng, Y. Tu, D.A. Wilson, Micro- and nano-motors for biomedical applications, *J Mater Chem B* 2 (17) (2014) 2395–2408.
- [33] L. Baraban, D. Makarov, R. Streubel, I. Mönch, D. Grimm, S. Sanchez, O.G. Schmidt, Catalytic Janus motors on microfluidic chip: deterministic motion for targeted cargo delivery, *ACS Nano* 6 (4) (2012) 3383–3389.
- [34] Z. Ghalanbor, S.-A. Marashi, B. Ranjbar, Nanotechnology helps medicine: Nanoscale swimmers and their future applications, *Med. Hypotheses* 65 (1) (2005) 198–199.
- [35] H. Wu, D. Zhong, Z. Zhang, Y. Wu, Y. Li, H. Mao, K. Luo, D. Kong, Q. Gong, Z. Gu, A bacteria-inspired morphology genetic biomedical material: self-propelled artificial microbots for metastatic triple negative breast cancer treatment, *ACS Nano* 15 (3) (2021) 4845–4860.
- [36] E. Lauga, A.M.J. Davis, Viscous Marangoni propulsion, *J. Fluid Mech.* 705 (2012) 120–133.
- [37] M. Sandoval, J.C. Hidalgo-Gonzalez, J.I. Jimenez-Aquino, Self-driven particles in linear flows and trapped in a harmonic potential, *Phys. Rev. E* 97 (3–1) (2018) 032603.
- [38] J.R. Baylis, J.H. Yeon, M.H. Thomson, A. Kazerooni, X. Wang, A.E. St John, E.B. Lim, D. Chien, A. Lee, J.Q. Zhang, J.M. Piret, L.S. Machan, T.F. Burke, N.J. White, C. J. Kastrup, Self-propelled particles that transport cargo through flowing blood and halt hemorrhage, *Science advances* 1(9) (2015) e1500379-e1500379.
- [39] M. Frenkel, A. Vilik, I. Legchenkova, S. Shoval, E. Bormashenko, Mini-generator of electrical power exploiting the marangoni flow inspired self-propulsion, *ACS Omega* 4 (12) (2019) 15265–15268.
- [40] J. Ou, K. Liu, J. Jiang, D.A. Wilson, L. Liu, F. Wang, S. Wang, Y. Tu, F. Peng, Micro-/nanomotors toward biomedical applications: the recent progress in biocompatibility, *Small* 16 (27) (2020) 1906184.
- [41] G. Janani, M. Kumar, D. Chouhan, J.C. Moses, A. Gangrade, S. Bhattacharjee, B.B. Mandal, Insight into silk-based biomaterials: from physicochemical attributes to recent biomedical applications, *ACS Appl. Bio Mater.* 2 (12) (2019) 5460–5491.

- [42] P. Kumar, S. Ebbens, X. Zhao, Inkjet printing of mammalian cells – Theory and applications, *Bioprinting* 23 (2021) e00157.
- [43] Q. Hu, Y. Ren, W. Liu, Y. Tao, H. Jiang, Simulation analysis of improving microfluidic heterogeneous immunoassay using induced charge electroosmosis on a floating gate, *Micromachines* 8 (7) (2017) 212.
- [44] A. Vilk, I. Legchenkova, M. Frenkel, E. Bormashenko, Spiral thermal waves generated by self-propelled camphor boats, *Condensed Matter* 5 (3) (2020) 51.
- [45] D.C. Venerus, D. Nieto Simavilla, Tears of wine: new insights on an old phenomenon, *Sci. Rep.* 5 (1) (2015) 16162.